

Metallic delafossite thin films for unique device applications

Takayuki Harada^{1,2,a)} and Yoshinori Okada³

¹ MANA, National Institute for Materials Science, 1-1 Namiki, Tsukuba, Ibaraki 305-0044, Japan

² JST, PRESTO, 4-1-8 Honcho, Kawaguchi, Saitama, 332-0012, Japan

³ Quantum Materials Science Unit, Okinawa Institute of Science and Technology (OIST), Okinawa 904-0495, Japan

^{a)} Correspondence to: HARADA.Takayuki@nims.go.jp

Metallic delafossites (ABO_2) are layered oxides with quasi-two dimensional conduction layers. Metallic delafossites are among the most conducting materials with the in-plane conductivity comparable with that of elemental metals. In this perspective, we will discuss basic properties and future research prospects of metallic delafossites, mainly focusing on thin films and heterostructures. We exemplify the fascinating properties of these compounds such as high conductivity and surface polarity and discuss how it can be utilized in thin films and heterostructures.

1. INTRODUCTION

Research on quantum materials has deepened our knowledge of condensed matter physics and expanded the choice of materials for future thin-film devices. Metallic delafossites $PdCoO_2$, $PdCrO_2$, $PdRhO_2$, and $PtCoO_2$, a family of materials that will be the focus of this perspective, are natural superlattices of two-dimensional (2D) conducting sheets and correlated insulating layers.¹⁻³ In the rigid oxide framework shown in Figure 1, metallic delafossites demonstrate intriguing physical properties driven by high electron mobility and surface polarity. These compounds are also chemically inert and thermally stable, with a decomposition temperature of $\sim 800^\circ C$ or higher in air.¹ The high stability of metallic delafossites give them great potential for use in thin-film devices.

After an overview of the basic properties of metallic delafossites (section 2), this paper will focus on two important characteristics of these materials with respect to device applications: high mobility/conductivity, which give rise to intriguing transport phenomena (section 3 and 4), and surface polarity, which leads to a large work function and emergent spin polarized surface states (section 5 and 6). While high mobility/conductivity and

surface polarity are essentially independent properties, metallic delafossites in characteristic layered crystal structures demonstrate these properties. The physical properties of metallic delafossites have mainly been revealed through the study of bulk single crystals⁴, with limited research on thin films. For metallic delafossites to be used for device applications, it will be crucial to accelerate research on thin films, which includes making heterostructures by design (section 6). For this purpose, as described in section 7, we emphasize the importance of direct imaging of metallic delafossite thin films using spectroscopic imaging scanning tunneling microscopy (SI-STM).

2. PHYSICAL PROPERTIES OF METALLIC DELAFOSSITES

In this section, a brief overview is given on the physical properties of metallic delafossites. For details, the reader can refer to existing reviews on single crystals,^{4, 5} thin films,⁶ and theory.⁷ As shown in Figure 1(a), the crystal structure of metallic delafossites consists of ionic layers of A^+ and $[BO_2]^-$ octahedra. At present, five compounds in the delafossite family have been shown to exhibit metallic

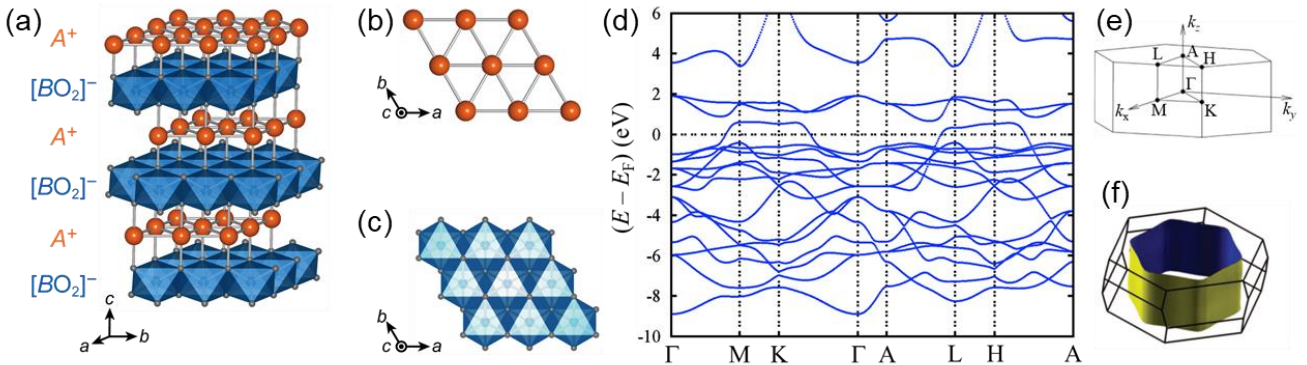


FIG. 1. (a) The crystal structure of metallic delafossites ABO_2 . The A^+ and $[BO_2]^-$ layers are noted. (b) The crystal structures of A^+ layers and (c) the $[BO_2]^-$ layers. (d) The electronic band structure, (e) the Brillouin zone of the hexagonal unit cell, and (f) the Fermi surface of $PdCoO_2$ calculated by density-functional theory (DFT) in the generalized gradient approximation (GGA).⁷⁹ Reprinted with permission from ACS (Copyright 2008, American Chemical Society)

electrical conduction: PdCoO₂, PdCrO₂, PdRhO₂, PtCoO₂, and AgNiO₂.⁴ Here, we will focus on the first four compounds, in which A⁺ (Pd⁺ or Pt⁺) ions mediate electrical conduction, and will refer to them collectively as metallic delafossites. Hereafter, we will not discuss AgNiO₂ as in this compound, the B-site Ni ions contribute to electrical conduction, resulting in considerably different physical properties from the other four compounds.⁸⁻¹⁰

In each layer, A⁺ ions or BO₆ octahedra form 2D triangular lattices (Fig. 1(a)–(c)). The A⁺ layers are 2D conductive sheets while the [BO₂][−] layers are insulating in nature. Because of this layered crystal structure, metallic delafossites show quasi-2D electrical conduction. Conductivity in the ab-plane (σ_{ab}) of metallic delafossites is generally orders of magnitude higher than along the c-axis (σ_c). In the case of PdCoO₂ at room temperature, $\sigma_{ab} \sim 3.8 \times 10^7$ S/m while $\sigma_c \sim 9.3 \times 10^4$ S/m. At cryogenic temperatures, the conductivity of PdCoO₂ increases by a factor of ~ 400 for σ_{ab} ,¹¹ resulting in an electron mean free path length $l \sim 21.4 \mu\text{m}$.^{4,12}

As will be discussed in section 3, the quasi-2D high-mobility electrons generate intriguing electrical transport phenomena as recently shown in high-purity single crystals.¹³⁻¹⁸ The band structure and Brillouin zone of PdCoO₂ is shown in Figures 1(d) and (e). The dispersive band that crosses the Fermi level is predominantly attributed to Pd 4d and Pd 5s states.¹⁹ These electronic states form the nearly cylindrical Fermi surface shown in Figure 1(f), reflecting the quasi-2D electrons in the Pd layers.

Regarding magnetic properties, PdCrO₂ shows antiferromagnetic transition with the Néel temperature $T_N \sim 37.5$ K while the bulk states of PdCoO₂, PdRhO₂, and PtCoO₂ are nonmagnetic.⁴ In PdCrO₂, the Cr³⁺ ions have localized spins with $S = 3/2$.^{20,21} As shown in Figure 1(c), the CrO₆ octahedra form geometrically frustrated 2D spin triangular lattices, which influence the high-mobility electrons in the Pd sheets and cause an unconventional anomalous Hall effect.²⁰ Although PdCoO₂, PdRhO₂, and PtCoO₂ are nonmagnetic in bulk because of the fully occupied t_{2g} -like orbitals, recent experiments have indicated the existence of spin-dependent electronic states at the surface, which will be discussed further in sections 5–7.²²⁻²⁴

3. HIGH MOBILITY AND HIGH DENSITY QUASI-2D ELECTRONS

As described in section 1, one of the most remarkable characteristics of metallic delafossites are their high electrical conductivity. Figure 2 compares the metallic delafossites and various high-mobility 2D electronic systems: 2D materials, quasi-2D materials, and 2D electrons at surfaces/interfaces (Figs 2(a)–(c)). As shown in Fig. 2(d), currently known high mobility electronic systems have relatively low carrier densities of $n_{2D} < 10^{14}$ cm^{−2}. In contrast, metallic delafossites, plotted in red in Fig. 2(d), are high mobility quasi-2D systems with comparably high carrier densities of $n_{2D} \sim 10^{15}$ cm^{−2}. Thus, metallic delafossites are unique and ideal for exploring mesoscopic electrical transport phenomena in high mobility, high carrier density materials (Fig. 2(d)).

To compare the cleanness of 2D conduction channels, mean free path l is plotted in Fig. 2(e) for the same set of data as Fig. 2(d). The mean free path of metallic

delafossites compares well with most of high-mobility materials, showing exceptional cleanness of the conduction channels of metallic delafossites (Fig. 2(e)). As demonstrated by PdCoO₂ single crystals at cryogenic temperatures, the 2D electrons in Pd sheets have impressively long electron scattering lengths, with an electron mean free path length $l \sim 21.4 \mu\text{m}$ ¹² and a phase coherence length $l_\phi > 10 \mu\text{m}$.¹⁷ An interesting consequent phenomenon observed for the high-mobility electrons in PdCoO₂ is hydrodynamic electron flow.¹³ The flow of electrons in solids is normally far different from the hydrodynamic flow of an ordinary fluid like water. In ordinary conductors, electrons are scattered by phonons and impurities, resulting in momentum relaxation and the generation of resistance. On the other hand, if the total momentum of electrons is conserved inside a conductor and is predominantly relaxed at the edges, electrical transport resembles the hydrodynamic motion of a fluid. To achieve this, the rate of momentum-relaxing scattering inside a conductor (electron-impurity, electron-phonon, and Umklapp scattering) should be minimized. In this situation, the channel resistance is partly given by the viscosity of electron fluid. The viscosity of electron fluid is governed by the rate of momentum-conserving electron-electron scattering. This was recently demonstrated by Moll and colleagues who fabricated microchannels in PdCoO₂ single crystals using a focused ion beam (FIB) technique.¹³ The low rate of momentum-relaxing scattering in ultrapure PdCoO₂ single crystals results in electrical transport through these microchannels that can be described as hydrodynamic motion.^{13, 25} Furthermore, various mesoscopic high mobility electrical transport phenomena, such as ballistic^{16, 18, 26} or phase-coherent transport¹⁷, have been demonstrated in high-purity single crystals of PdCoO₂.

Along with the above-mentioned transport phenomena, the high carrier density in metallic delafossites is predicted to cause additional physical effects. Because of the high carrier density, the Fermi surfaces of metallic delafossites are considerably larger than other quasi-2D systems, such as semiconductor heterostructures (Fig. 1(f)). This can cause the many-body effects, such as quasiparticle formation and/or an anisotropic Fermi surface shape, to appear with the high mobility transport phenomena. For example, because of the large hexagonal cylindrical Fermi surface, the trajectory of ballistic transport is not isotropic as in ordinary 2D systems but highly directional and dominantly oriented in six directions (Fig. 3(a), (b)).^{16, 18, 26} Identifying exotic consequences of many-body effects in mesoscopic electrical transport is an intriguing challenge, which may be facilitated by real-space probing techniques (section 7).

While mesoscopic electrical transport phenomena in metallic delafossites have been mainly studied in FIB-patterned bulk single crystals, these fascinating transport properties are motivating thin-film researchers to grow high-purity PdCoO₂ in order to make mesoscopic devices using conventional lithography techniques. Once realized, exotic transport in thin films could be expanded to the study of spin transport or the superconducting proximity effect by making thin-film heterostructures, as will be discussed in section 6 and 7. Signatures of phase-coherent transport in PdCoO₂ thin films have already been reported in mesoscopic structures.²⁷ Although the l_ϕ and l of thin-

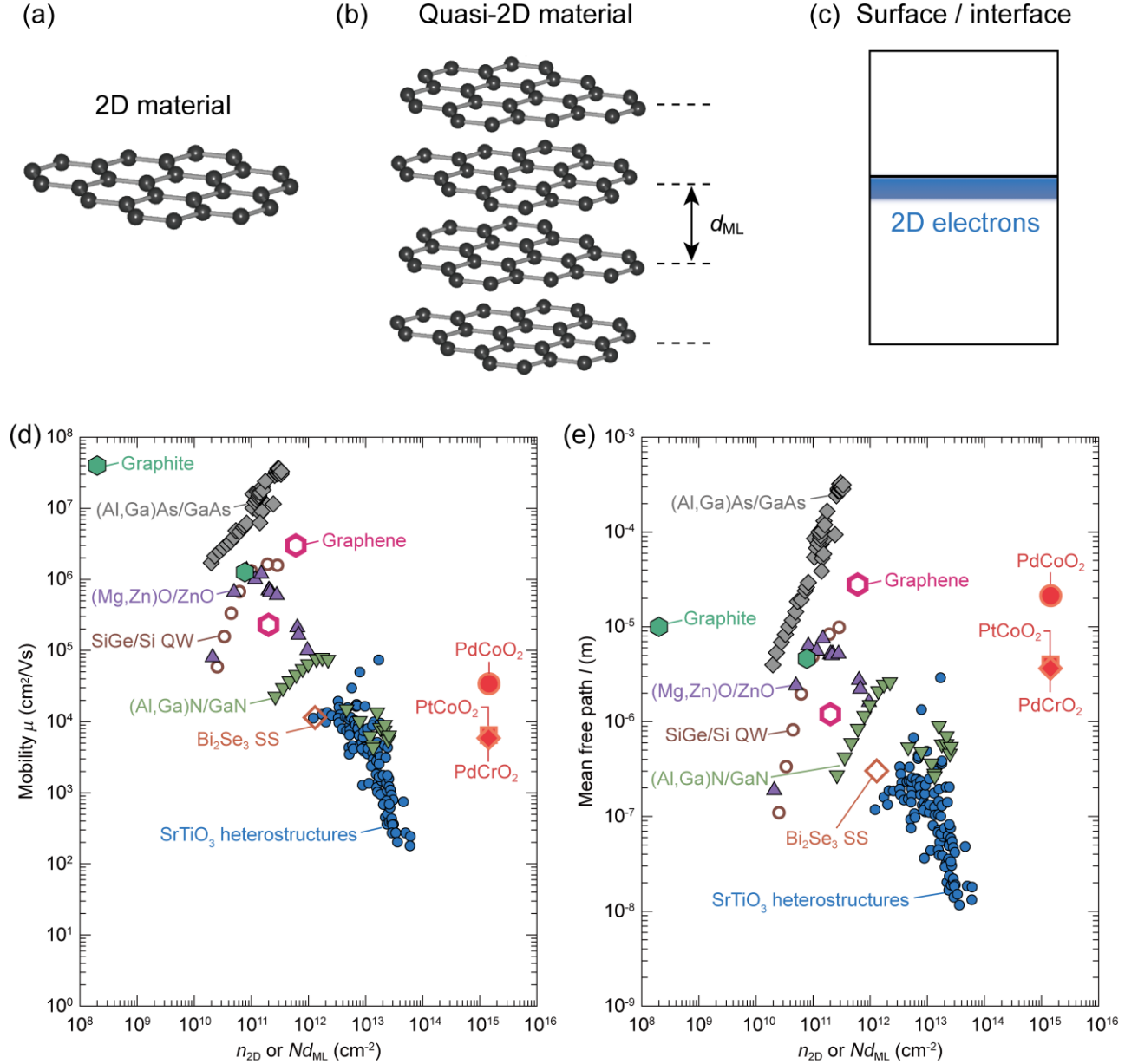


FIG. 2. Comparison of various (quasi-)2D high mobility electronic systems. The schematics of (a) 2D material, (b) quasi-2D material, and (c) 2D electrons at a surface/interface. (d) Charge carrier mobility μ of selected materials. 2D materials: suspended graphene at ~ 5 K⁸⁰ and graphene on h-BN below 130 K (open magenta hexagons).^{80, 81} Quasi-2D materials: bulk single crystals of PdCoO₂ (red circle), PtCoO₂ (red square), and PdCrO₂ (red diamond) at 4 K¹² and graphite (green hexagon) at 4.2 K^{82, 83} or 3 K.⁸⁴ Semiconductor interfaces: (Al,Ga)As/GaAs heterostructures (black diamonds),^{85, 86} SiGe/Si quantum wells (QW, brown open circles) at 0.3 K,⁸⁷ (Mg,Zn)O/ZnO heterostructures (purple up-pointing triangles) at 500 mK or ≤ 100 mK,⁸⁸ (Al,Ga)N/GaN heterostructures (green down-pointing triangles) at 20 K⁸⁹ or 0.3 K,⁹⁰ and SrTiO₃-based heterostructures (blue circles) at low temperature.⁹¹ Surfaces of topological insulators: the surface states (SS) of Bi₂Se₃ at 1.5 K.⁹² For the quasi-2D systems, the sheet carrier density for a single conductive layer is calculated as $n_{2D} = Nd_{ML}$ using the carrier concentration N and the interlayer distance d_{ML} schematically shown in (b). The carrier mobility of PdCoO₂, PtCoO₂, and PdCrO₂ are calculated as $\mu = 1/eN\rho$, where e is elemental charge and ρ is resistivity. The reported *ab*-plane resistivity is used for ρ . (e) Mean free path l of charge carriers in the same materials as (d). For graphene and graphite, we used the reported values of l in the literature.^{80-82, 84} For the other materials, the mean free path l is calculated using the formulas for circular Fermi surfaces around valleys: $l = \frac{\hbar k_F \mu}{e}$ and $k_F = \left(\frac{4\pi n_{2D}}{g_s g_v} \right)^{\frac{1}{2}}$, where \hbar is the reduced Planck constant, k_F is the Fermi wave vector, g_s is the spin degeneracy, and g_v is the valley degeneracy. For SrTiO₃ heterostructures, the non-circular 2D Fermi surface could result in deviation from the calculated l . We also note that the mean free path is proposed to be limited by the sample size for the graphene data.^{80, 81}

film mesoscopic structures are currently $l_\phi \sim 100$ nm and $l \sim 10$ nm,²⁷ improving thin film quality could extend these scattering lengths.

4. TOWARD THIN FILMS WITH HIGH ELECTRON MOBILITY

In this section, we will discuss the possibility of achieving high electron mobility metallic delafossite thin

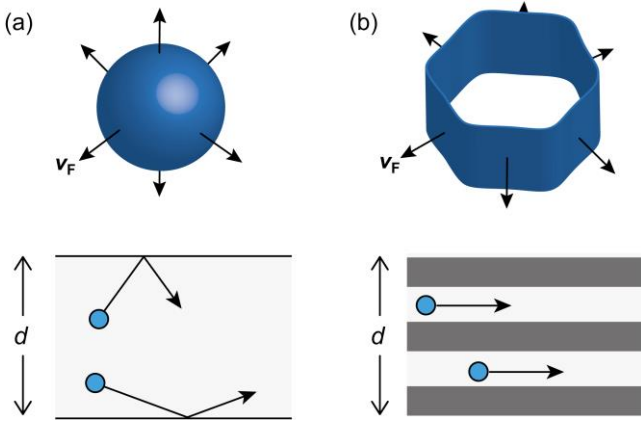


FIG. 3. (a) A spherical Fermi surface (top) and a schematic of electrons travelling with v_F in a thin film with thickness d (bottom). (b) A schematically drawn hexagonal Fermi surface of PdCoO₂ (top) and electrons travelling with v_F along the conductive layer of Pd (bottom). The total thickness of the thin film is noted as d . We note that the warping in the PdCoO₂ Fermi surface results in finite component of v_F perpendicular to the conductive layer.

films. Metallic delafossite thin films were first fabricated in the 1980s by annealing amorphous precursors deposited by sputtering.²⁸ Recently, several groups have reported the fabrication of c -axis oriented thin films of PdCoO₂,²⁹⁻³³ PdCrO₂,³³⁻³⁵ and PtCoO₂³³ by pulsed laser deposition (PLD),^{29, 31, 34} molecular beam epitaxy,^{30, 32} and solution-based processes.³³

Is it possible to increase the electron mobility of thin films to the level of single crystals? With the exception of metallic delafossites, studies on the resistivity of thin metal films have a long history. Studies on elemental metals such as Au,³⁶ Pt,³⁷ Co,³⁸ and Cu^{39, 40} have shown that the resistivity of metals scales with thin film thickness and generally increases as thickness is reduced down to a few nanometers, which can be explained by the surface scattering of electrons. According to theory, the resistivity, ρ , of three-dimensional metals is expected to increase as the thickness, d , decreases, with $\rho \propto 1/[d \ln(l_{\text{bulk}}/d)]$,^{41, 42} $\rho \propto 1/d$,⁴⁰ or $\rho \propto 1/d^2$,⁴³⁻⁴⁵ depending on the model, where l_{bulk} is the bulk mean free path.

Because of the quasi-2D nature of PdCoO₂, a reduction in thickness may not cause a serious surface scattering effect since electron mobility could be maintained, as seen in other quasi-2D systems like graphite. The directional transport effect found in single crystals of PdCoO₂ is an encouraging result that supports this hypothesis. According to transport measurements of PdCoO₂ single crystals,^{16, 18, 26} the ballistic transport of electrons is highly anisotropic, reflecting the hexagonal cylindrical shape of the Fermi surface. The spherical Fermi surfaces of alkali metals are compared with those of PdCoO₂ in Figure 3(a) and (b).

The velocity of electrons, v_n , is expressed as,

$$v_n(\mathbf{k}) = \frac{1}{\hbar} \nabla_{\mathbf{k}} \varepsilon_n(\mathbf{k})$$

, where n is the band index, \mathbf{k} is the wavevector, \hbar is the reduced Planck constant, and $\varepsilon_n(\mathbf{k})$ is the energy of an electron with \mathbf{k} in the n -th band.⁴⁶ The Fermi velocity, v_F , is therefore perpendicular to the Fermi surface and is isotropic in alkali metals that has additional one electron to

the closed-shell configuration. In contrast, the v_F of PdCoO₂ is dominantly oriented in six directions in the ab -plane (Fig. 3, top). Because of the directional ballistic transport, c -axis oriented thin films of metallic delafossites may not be significantly affected by surface scattering (Fig. 3, bottom). Although the warping in the Fermi surface of PdCoO₂ causes a finite component of v_F and sets a limitation to the above discussion,⁴⁷ the nearly cylindrical Fermi surface of PdCoO₂ should be a predominant advantage for achieving long mean free path in thin films.

Table 1 summarizes the challenges toward high-mobility thin films of metallic delafossites and reported approaches. So far, PdCoO₂ is most studied for thin films among the metallic delafossites. The typical growth condition of PdCoO₂ for PLD is the substrate temperature of 620–700°C and the oxygen pressure of 0.1–1.7 Torr.^{29, 31} For MBE growth, the substrate temperature ranges in 300–480°C under atomic oxygen plasma³⁰ or distilled ozone.³² The room-temperature ab -plane resistivity ρ_{ab} of the PdCoO₂ thin films reported to date is about 2-5 times higher than that of the bulk single crystal ($\rho_{ab} = 2.6 \mu\Omega\text{cm}$).^{6, 29} The low-temperature resistivity has been reported for these thin films. The largest residual resistivity ratio (RRR) for PdCoO₂ of 16 has been reported in a thick (~180 nm) MBE-grown PdCoO₂ thin film that is post-annealed at 800 °C in oxygen.³⁰ The RRR of 16 in the PdCoO₂ thin film is still small compared with the bulk value ($RRR \sim 400$).¹¹

To improve the thin-film quality, dominant scattering sources should be clarified. One of the possible dominant scattering sources is twin boundaries. For c -axis oriented thin-film growth of metallic delafossites, Al₂O₃ substrates are widely used. As the surface of Al₂O₃ substrates is effectively 6-fold symmetric, the reported thin films have crystal twins that are 180°-rotated from each other.^{29, 30, 32} These twin boundaries can scatter electrons. Growing single crystal thin films without twin boundaries could dramatically improve electron mobility. Although various promising approaches, as listed in Table 1, to achieve this using single crystal substrates with delafossite structures⁴⁸ or twin-free delafossite buffer layers⁴⁹ have been reported, twin-free thin films have not realized. Toward twin-free thin films, stacking faults need to be also suppressed.

Other possible scattering sources include point defects caused by impurities, cation off stoichiometry, and oxygen vacancies. As the RRR of thin films have not been significantly dependent on the purity of the material sources (PLD targets, MBE sources),^{32, 50} impurity scattering seems not a dominant scattering mechanism in the current metallic delafossite thin films. Increase of RRR by post annealing could be due to the reduction of oxygen vacancies as well as improved atomic ordering in the crystal. Post-annealing temperature is limited by the decomposition temperature of metallic delafossites (800-925°C). Alternative approach such as thin-film growth techniques based on chemical reactions could be promising to improve atomic ordering as they may mimic the bulk synthesis of pure single crystals.^{33, 51}

As a potentially low-cost and wide-area deposition technique that is important for application, solution-based growth on 2-inch wafers has been reported for PdCoO₂, PdCrO₂, PtCoO₂.³³ Regarding device fabrication, PdCoO₂ has been successfully patterned into submicron scales by conventional electron beam lithography and Ar-ion

Table 1. Challenges in growth and processing of metallic delafossite thin films and tested approach

Growth/processing challenges	Tested approach	Applied materials
Twinning	Miscut substrates ³¹	PdCoO ₂
	Substrates with low symmetry surfaces	
	β -Ga ₂ O ₃ (-201) (ref. ⁵⁵)	PdCoO ₂ , PdCrO ₂
	SrTiO ₃ (111) (ref. ⁴⁹)	PdCrO ₂
	Buffer layers: CuCrO ₂ (ref. ^{34, 49})	PdCrO ₂
	Delafossite-type substrates: CuFeO ₂ (ref. ⁴⁸)	–
Stacking faults	Observed by HAADF-STEM ^{27, 30}	PdCoO ₂
Impurities	PLD with high purity targets (PdCoO ₂ 4N5, Pd 5N) ⁵⁰	PdCoO ₂
	MBE with high purity sources (Pd 5N, Co 4N5) ³²	PdCoO ₂
Cation stoichiometry	Alternate ablation of PdCoO ₂ and PdO _x in PLD ²⁹	PdCoO ₂
	MBE growth ^{30, 32}	PdCoO ₂
Oxygen vacancies	Post annealing in air or O ₂ improves <i>RRR</i> (ref. ³⁰)	PdCoO ₂
	MBE in atomic oxygen plasma ³⁰ or ozone ³²	PdCoO ₂
Atomic ordering	Post annealing in air or O ₂ improves <i>RRR</i> (ref. ³⁰)	PdCoO ₂
	Chemical growth method	
	Solution-based growth ³³	PdCoO ₂ , PdCrO ₂ , PtCoO ₂
	Atomic layer deposition ⁵¹	PtCoO ₂
Lattice matching (<i>ab</i> -plane and <i>c</i> -axis)	Buffer layers: CuCrO ₂ (ref. ^{34, 49})	PdCrO ₂
	Delafossite-type substrates: CuFeO ₂ (ref. ⁴⁸)	–
Wide area	Solution-based growth on 2-inch wafers ³³	PdCoO ₂ , PdCrO ₂ , PtCoO ₂
Heterostructures	Schottky junctions with β -Ga ₂ O ₃ (ref. ^{35, 55-57})	PdCoO ₂ , PdCrO ₂
Microfabrication	Electron beam lithography and Ar ion milling ²⁷ Resist: HSQ, Line width: ~100 nm	PdCoO ₂

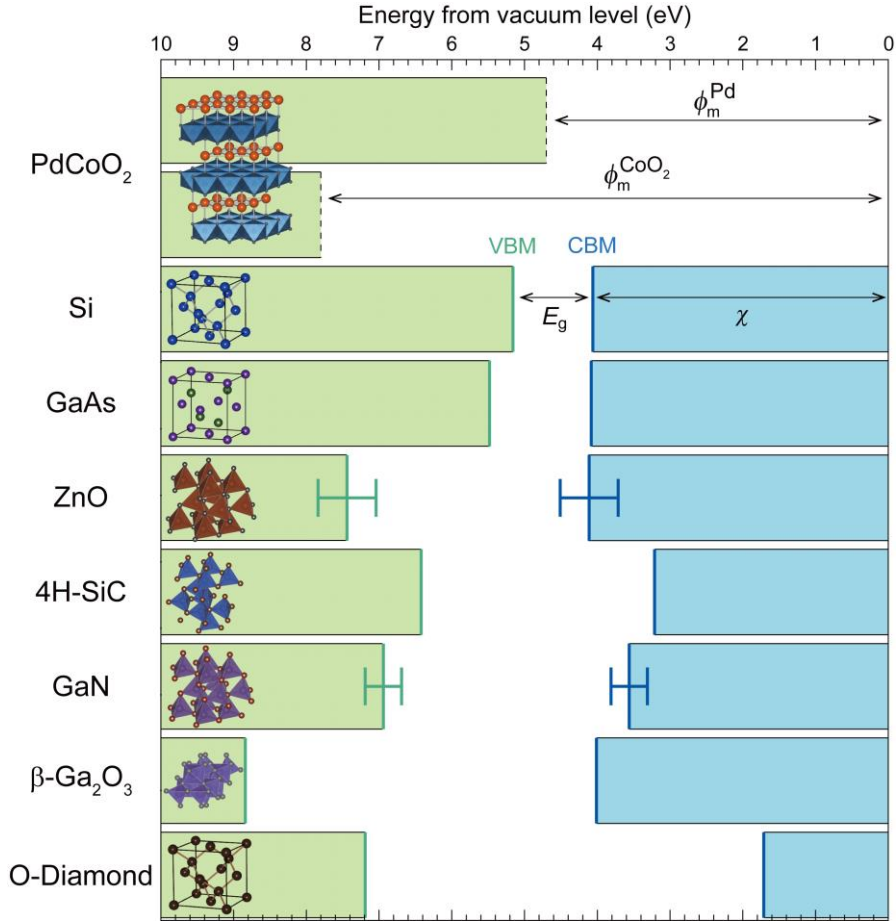


FIG. 4. The band alignment of semiconductors compared with the work function of Pd-terminated (ϕ_m^{Pd})^{53, 55} and CoO₂-terminated ($\phi_m^{\text{CoO}_2}$)⁵³ PdCoO₂. The valence and conduction bands of the various semiconductors are shown in green and blue, respectively. For Si, the electron affinity (χ), the bandgap (E_g), the conduction band minimum (CBM), and the valence band maximum (VBM) are noted. The band alignment is drawn based on the reported bandgap and the electron affinity for Si,⁹³ GaAs,⁹³ ZnO,^{93, 94} 4H-SiC,⁹⁵ GaN,⁹⁶ β -Ga₂O₃,^{97, 98} and oxidized diamond surfaces.^{99, 100} For ZnO and GaN, the CBM and VBM are shown with bars, which are reported to depend on the surface termination.^{94, 96}

milling.²⁷ As discussed in the sections 5 and 6, search for novel heterostructures is important to find a possible application of metallic delafossites.

5. POLAR SURFACES FOR DEVICE APPLICATIONS

Along with high electron mobility/conductivity, the surface polarity of metallic delafossites is also highly significant as it permits an exceptionally large work function, which is beneficial for device applications. According to the classification by Tasker,⁵² the *c*-plane surfaces of metallic delafossites are classified as type-3 polar surfaces.⁶ As a result, the surface properties of metallic delafossites strongly depend on the termination layer of the surface (e.g., Pd or CoO₂ layer). Recent surface measurements of cleaved PdCoO₂ showed that the work function of a Pd-terminated surface (ϕ_m^{Pd}) was ~ 4.7 eV while a CoO₂-terminated surface ($\phi_m^{\text{CoO}_2}$) was ~ 7.8 eV, indicating that the work function of PdCoO₂ is highly dependent on the termination layer.⁵³ The large difference between ϕ_m^{Pd} and $\phi_m^{\text{CoO}_2}$ is due to the polar surface. A work function of ~ 7.8 eV is very large for a metallic compound and far exceeds the Pt work function (~ 5.65 eV), which is the largest value found in elemental metals.⁵⁴

The large work function of PdCoO₂ should be of great value for various device applications, such as for electrodes for semiconductor devices. In Figure 4, the work function of PdCoO₂ (ϕ_m^{Pd} and $\phi_m^{\text{CoO}_2}$) is compared with the conduction band minimum (CBM) and valence band maximum (VBM) of various semiconductors. In semiconductor devices, Schottky junctions formed at metal/semiconductor interfaces often play key roles in device operation. According to the Schottky-Mott relationship, the ideal Schottky barrier height of metal/*n*-type semiconductor interfaces, $\phi_{b,n}$, is estimated to be $\phi_{b,n} = \phi_m - \chi$, where ϕ_m is the work function of a metal and χ is the electron affinity of a semiconductor. As shown in Figure 4, the difference between $\phi_m^{\text{CoO}_2}$ and χ of various semiconductors is as large as several eV. Therefore, large Schottky barrier heights can be achieved in PdCoO₂/*n*-type semiconductor polar interfaces, as demonstrated by PdCoO₂/ β -Ga₂O₃⁵⁵⁻⁵⁷ and PdCrO₂/ β -Ga₂O₃ junctions.³⁵ The large Schottky barrier height would be useful for diodes for high-temperature operation and Schottky gates for transistors. Careful control of the initial growth layer would be important to generate an interface with a homogeneous Schottky barrier height.

In general, ohmic contacts with low contact resistance are important to reduce power loss in wide bandgap semiconductor devices. Making low resistance contacts to p-type wide bandgap semiconductors is often a challenge, particularly when the hole concentration is low. In the Schottky-Mott relationship, the Schottky barrier height of a metal/p-type semiconductor interface is $\phi_{b,p} = \chi + E_g - \phi_m$, where E_g is the bandgap of the semiconductor. To achieve a true ohmic contact ($\phi_{b,p} < 0$), one needs a metal with $\phi_m > \chi + E_g$. For wide bandgap semiconductors such as 4H-SiC ($E_g \sim 3.2$ eV) and GaN ($E_g \sim 3.4$ eV), $\chi + E_g$ is well above 6 eV, and there is no elemental metal electrode that satisfies $\phi_m > \chi + E_g$. As shown in Figure 4, PdCoO₂ with a CoO₂ initial layer is a promising candidate for a true ohmic contact for wide bandgap semiconductors since $\phi_m^{\text{CoO}_2}$ is larger than the $\chi + E_g$ of semiconductors with p-type doping (Si, GaAs, ZnO, 4H-SiC, GaN, and diamond).

6. SURFACE SPIN STATES

Surface polarity also causes emergent spin polarized surface states. In general, to electrostatically stabilize the polar surface, charge compensation occurs.^{52, 58, 59} This causes the electron density at the surface to differ from that of the inner bulk. Recent experiments have indicated that charge compensation changes the surface of the inherently nonmagnetic PdCoO₂ to have spin-dependent electronic states.

The surface electronic states of PdCoO₂ have been calculated using a density functional theory (DFT)-based method.⁶⁰ Owing to the electronic reconstruction induced by the surface polarity, a Pd-terminated surface of PdCoO₂ was proposed to have surface magnetism.⁶⁰ The calculation also predicted that the Co-derived bands at a CoO₂-terminated surface are split because of the spin-orbit interaction.⁶⁰

Sunko and colleagues observed the BO₂-terminated surfaces of PdCoO₂, PtCoO₂, and PdRhO₂ by angle-resolved photoemission spectroscopy (ARPES) and discovered Rashba-like spin splitting,²² which is caused by strong inversion symmetry breaking on the BO₂-terminated surface. Spin splitting is comparable to atomic spin-orbit coupling of B-site cations. Mazzola *et al.* reported the surface ferromagnetic states at Pd-terminated surfaces of PdCoO₂ by ARPES.²³ Ferromagnetism has also been detected in PLD-grown PdCoO₂ thin films by ARPES and the anomalous Hall effect.²⁴ From the magnetoresistance measurements under the in-plane magnetic field, the Pd-terminated surface of PdCoO₂ also has Rashba-spin splitting with a Rashba coefficient $\sim 0.75 \pm 0.3$ eV.⁶¹ Possible coexistence of ferromagnetism and Rashba spin-orbit coupling will be an interesting subject for future studies in the context of spin-orbitronics.⁶²

Here we will discuss the prospects of using the Rashba ferromagnetic surfaces of metallic delafossites. We performed DFT calculations of a Pt-terminated PtCoO₂ surface (Fig. 5) and found similar properties to that of PdCoO₂. In the nonmagnetic calculation, Rashba-like split bands were observed around the Γ point. Furthermore, the flat region of the conduction band shifted close to the Fermi level, which may cause Stoner splitting, as with PdCoO₂.²³ In the calculation considering collinear spin polarization, the bands around the Γ point were spin-split. The Rashba effect visible in the nonmagnetic calculation was more

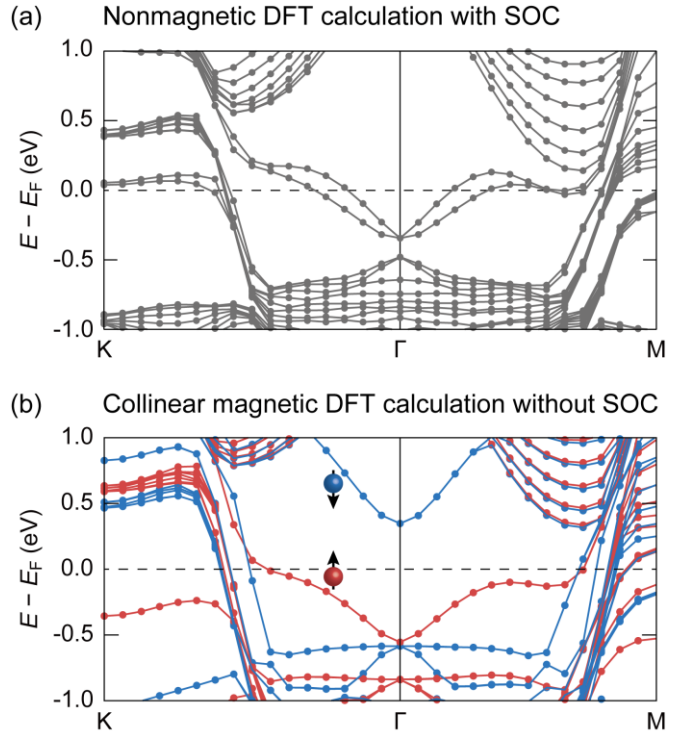


FIG. 5. The electronic structure of the slab model for a Pt-terminated PtCoO₂, calculated by density functional theory (DFT) using the CASTEP package. The vertical axis is the energy relative to the Fermi level (E_F). (a) The nonmagnetic calculation result considering spin-orbit coupling (SOC). (b) The calculation result considering collinear spin polarization. The red and blue lines correspond to the spin-up and spin-down states, respectively. For (b), SOC is not included because of the limitation of our computer setup. Including spin-orbit interaction can give rise to non-collinear spin textures and require larger supercells for calculation. A symmetric slab model containing nine Pt and eight CoO₂ layers with a vacuum gap of 15 Å is employed for the calculation, following a report on PdCoO₂.²³ The inner five Pt and four CoO₂ layers are fixed to have the lattice constants of bulk single crystals.⁴ The outer four Pt and four CoO₂ layers were relaxed. For both (a) and (b), the generalized gradient approximation and Perdew-Burke-Ernzerhof (GGA-PBE) functionals are used, and the Hubbard U is not taken into account.

pronounced in PtCoO₂ compared with that in PdCoO₂ because of the larger atomic spin-orbit coupling in Pt than in Pd (Fig. 5(a)).

Surface spin-split electronic states can be utilized in heterostructures to induce exotic electronic states. For example, making a heterostructure with a superconductor may be interesting. As a model system that could show topological superconductivity, a 2D electronic system with relatively large spin-orbit coupling, effective Zeeman coupling, and proximity-induced superconductivity has been proposed.^{63, 64} The model Hamiltonian can be written as $H(k) = H_0(k) + H_R(k) + H_Z + H_S$, where H_0 is kinetic energy, H_R is the Rashba spin-orbit interaction, H_Z is the effective Zeeman interaction, and H_S is the spin-singlet s -wave pair potential.⁶⁴ At the surface of PtCoO₂ or PdCoO₂, there can be a relatively large spin-orbit coupling $H_R(k)$ and

Stoner splitting (i.e., effective Zeeman coupling, H_Z) in a nearly 2D conduction channel. Inducing superconductivity H_S by the proximity effect and applying a magnetic field to adjust H_Z might induce topological superconducting states.

7. REAL SPACE PROBING OF ELECTRONIC STATES

To search for exotic electronic states in metallic delafossite, it is important to understand the external magnetic field dependence of electronic states. An ideal experimental approach for this purpose is SI-STM, which has a unique capability to resolve differential conductance ($dI/dV(r,E,B)$) that is proportional to the density of state below and above E_F , as a function of position r with atomic precision, energy E , and magnetic field B .⁶⁵⁻⁷⁰ SI-STM has been applied to the polar surfaces of PdCoO₂ bulk single crystals. On CoO₂-terminated surfaces of PdCoO₂, long-lived quasiparticle states have been visualized as extended six-fold standing waves.⁵³ This observation is consistent with the anisotropic hexagonal cylindrical Fermi surface of high mobility electrons (Fig. 3(b)). The observed standing waves have been interpreted by considering the large Rashba-like band splitting driven by strong inversion symmetry breaking.⁵³ On Pd-terminated surfaces of PdCoO₂, SI-STM has revealed the formation of charge density waves⁷¹ and renormalized electronic states that are coupled with magnons.⁷²

To further understand the electronic states of PdCoO₂ surfaces, SI-STM under external magnetic fields would be informative. As discussed in section 6, metallic delafossites are expected to contain characteristic surface spin states. On Pd-terminated surfaces of PdCoO₂ (and possibly in PtCoO₂), the possible coexistence of H_R and H_Z may give rise to spin-momentum coupled electronic structures with a H_Z -derived gap at the band crossing point (Fig. 5). Such spin-momentum coupled band structures with surface ferromagnetism could respond to external magnetic fields with controlled magnitude and direction.⁷³ For example, studies on magnetic-field dependent standing wave patterns and spatially averaged $dI/dV(E)$ shapes could reveal the spin-momentum coupled states of PdCoO₂. As SI-STM can visualize spin texture with atomic resolution in real space⁷⁵⁻⁷⁸, searching for topological magnetism on the surface of metallic delafossites is an exciting prospect.

To the best of our knowledge, all SI-STM studies reported to date were performed on cleaved surfaces of single crystals. By applying SI-STM to metallic delafossite thin films (Fig. 6), we would be able to investigate the electronic states of heterostructures with other materials, such as the superconductors discussed in section 6. Furthermore, as with other layered materials, monolayer-thick metallic delafossites may also be an interesting system for SI-STM study.

Finally, another important task is to identify the scattering sources that limit electron mobility of thin films. The electronic scattering response to twin-domain boundaries and point defects could be visualized by SI-STM, which would provide feedback for thin-film growth optimization. The combination of thin-film growth and real-space imaging techniques may lead to high-mobility thin films, facilitating research into unexplored phenomena in ultrathin films and heterostructures.

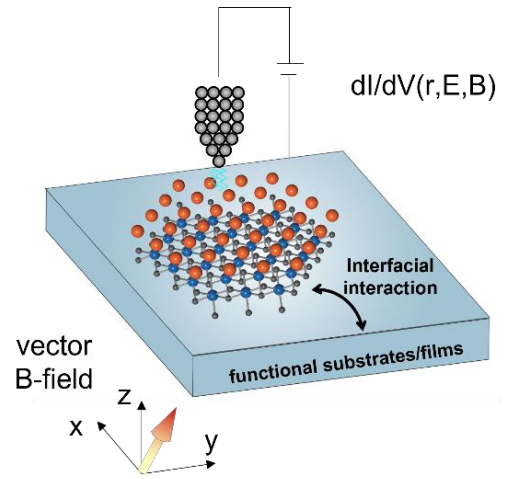


FIG. 6. A conceptual figure for spectroscopic imaging scanning tunneling microscopy (SI-STM) on metallic delafossite thin films and heterostructures. SI-STM is able to visualize electronic states with ultra-high spatial and energy resolution under controlled external magnetic fields.

8. CONCLUSION

In this article, we have provided an overview of the physical properties of metallic delafossites and discussed the perspectives of thin-film research. Inherent high mobility and surface polarity make metallic delafossites fascinating materials for both basic and application studies. In particular, mesoscopic electrical transport, many-body effects derived from Fermiology, and the interplay of these may lead to intriguing unexplored phenomena. Thin film growth of metallic delafossites would provide tremendous research possibilities for the design of heterostructures and functional devices.

Acknowledgments

The author would like to thank Prof. A. Tsukazaki and all collaborators for their contributions to this work on metallic delafossites. This work was supported by a Grant-in-Aid for Scientific Research (B) (20H02611), a Grant-in-Aid for Challenging Research (exploratory) (20K21138) from the Japan Society for the Promotion of Science (JSPS), MEXT Leading Initiative for Excellent Young Researchers (JPMXS0320200047), JST PRESTO (JPMJPR20AD), Izumi Science and Technology Foundation, and the Foundation for The Promotion of Ion Engineering.

Reference

1. R. D. Shannon, D. B. Rogers and C. T. Prewitt, *Inorg. Chem.* **10**, 713-718 (1971).
2. C. T. Prewitt, R. D. Shannon and D. B. Rogers, *Inorg. Chem.* **10**, 719-723 (1971).
3. D. B. Rogers, R. D. Shannon, C. T. Prewitt and J. L. Gillson, *Inorg. Chem.* **10**, 723-727 (1971).
4. A. I. Coldea, L. Seabra, A. McCollam, A. Carrington, L. Malone, A. F. Bangura, D. Vignolles, P. G. v. Rhee, R. D. McDonald, T. Sorgel, M. Jansen, N. Shannon and R. Coldea, *Phys. Rev. B* **90**, 020401 (2014).
5. R. Daou, R. Frésard, V. Eyert, S. Hébert and A. Maignan, *Sci. Technol. Adv. Mater.* **18**, 919-938 (2017).
6. T. Harada, *Materials Today Advances* **11**, 100146 (2021).
7. F. Lechermann, *npj Computational Materials* **7**, 120 (2021).
8. Y. J. Shin, J. P. Doumerc, P. Dordor, C. Delmas, M. Pouchard and P. Hagenmuller, *J. Solid State Chem.* **107**, 303-313 (1993).
9. A. I. Coldea, A. Carrington, R. Coldea, L. Malone, A. F. Bangura, M. D. Johannes, I. I. Mazin, E. A. Yelland, J. G. Analytis, J. A. A. J. Perenboom, C. Jaudet, D. Vignolles, T. Sorgel and M. Jansen, arXiv:0908.4169 (2009).
10. A. I. Coldea, L. Seabra, A. McCollam, A. Carrington, L. Malone, A. F. Bangura, D. Vignolles, P. G. v. Rhee, R. D. McDonald, T. Sorgel, M. Jansen, N. Shannon and R. Coldea, *Phys. Rev. B* **90**, 020401 (2014).
11. H. Takatsu, S. Yonezawa, S. Mouri, S. Nakatsuji, K. Tanaka and Y. Maeno, *J. Phys. Soc. Jpn.* **76**, 104701 (2007).
12. C. W. Hicks, A. S. Gibbs, A. P. Mackenzie, H. Takatsu, Y. Maeno and E. A. Yelland, *Phys. Rev. Lett.* **109**, 116401 (2012).
13. P. J. W. Moll, P. Kushwaha, N. Nandi, B. Schmidt and A. P. Mackenzie, *Science* **351**, 1061-1064 (2016).
14. N. Kikugawa, P. Goswami, A. Kiswandhi, E. S. Choi, D. Graf, R. E. Baumbach, J. S. Brooks, K. Sugii, Y. Iida, M. Nishio, S. Uji, T. Terashima, P. M. C. Rourke, N. E. Hussey, H. Takatsu, S. Yonezawa, Y. Maeno and L. Balicas, *Nat. Commun.* **7**, 10903 (2016).
15. N. Nandi, T. Scaffidi, P. Kushwaha, S. Khim, M. E. Barber, V. Sunko, F. Mazzola, P. D. C. King, H. Rosner, P. J. W. Moll, M. König, J. E. Moore, S. Hartnoll and A. P. Mackenzie, *npj Quantum Materials* **3**, 66 (2018).
16. M. D. Bachmann, A. L. Sharpe, A. W. Barnard, C. Putzke, M. König, S. Khim, D. Goldhaber-Gordon, A. P. Mackenzie and P. J. W. Moll, *Nat. Commun.* **10**, 5081 (2019).
17. C. Putzke, M. D. Bachmann, P. McGuinness, E. Zhakina, V. Sunko, M. Konczykowski, T. Oka, R. Moessner, A. Stern, M. König, S. Khim, A. P. Mackenzie and P. J. W. Moll, *Science* **368**, 1234-1238 (2020).
18. P. H. McGuinness, E. Zhakina, M. König, M. D. Bachmann, C. Putzke, P. J. W. Moll, S. Khim and A. P. Mackenzie, *Proc. Natl. Acad. Sci. U.S.A.* (2021).
19. M. Tanaka, M. Hasegawa, T. Higuchi, T. Tsukamoto, Y. Tezuka, S. Shin and H. Takei, *Physica B* **245**, 157-163 (1998).
20. H. Takatsu, S. Yonezawa, S. Fujimoto and Y. Maeno, *Phys. Rev. Lett.* **105**, 137201 (2010).
21. H. Takatsu, G. Nénert, H. Kadowaki, H. Yoshizawa, M. Enderle, S. Yonezawa, Y. Maeno, J. Kim, N. Tsuji, M. Takata, Y. Zhao, M. Green and C. Broholm, *Phys. Rev. B* **89**, 104408 (2014).
22. V. Sunko, H. Rosner, P. Kushwaha, S. Khim, F. Mazzola, L. Bawden, O. J. Clark, J. M. Riley, D. Kasinathan, M. W. Haverkort, T. K. Kim, M. Hoesch, J. Fujii, I. Vobornik, A. P. Mackenzie and P. D. C. King, *Nature* **549**, 492-496 (2017).
23. F. Mazzola, V. Sunko, S. Khim, H. Rosner, P. Kushwaha, O. J. Clark, L. Bawden, I. Marković, T. K. Kim, M. Hoesch, A. P. Mackenzie and P. D. C. King, *Proc. Natl. Acad. Sci. U.S.A.* **115**, 12956-12960 (2018).
24. T. Harada, K. Sugawara, K. Fujiwara, M. Kitamura, S. Ito, T. Nojima, K. Horiba, H. Kumigashira, T. Takahashi, T. Sato and A. Tsukazaki, *Phys. Rev. Res.* **2**, 013282 (2020).
25. G. Varnavides, Y. Wang, P. J. W. Moll, P. Anikeeva and P. Narang, arXiv:2106.00697 (2021).
26. M. D. Bachmann, A. L. Sharpe, A. W. Barnard, C. Putzke, T. Scaffidi, N. Nandi, S. Khim, M. König, D. Goldhaber-Gordon, A. P. Mackenzie and P. J. W. Moll, arXiv:2103.01332 (2021).
27. T. Harada, P. Bredol, H. Inoue, S. Ito, J. Mannhart and A. Tsukazaki, *Phys. Rev. B* **103**, 045123 (2021).
28. P. F. Carcia, R. D. Shannon, P. E. Bierstedt and R. B. Flippin, *J. Electrochem. Soc.* **127**, 1974-1980 (1980).
29. T. Harada, K. Fujiwara and A. Tsukazaki, *APL Mater.* **6**, 046107 (2018).
30. M. Brahlek, G. Rimal, J. M. Ok, D. Mukherjee, A. R. Mazza, Q. Lu, H. N. Lee, T. Z. Ward, R. R. Unocic, G. Eres and S. Oh, *Phys. Rev. Mater.* **3**, 093401 (2019).
31. P. Yordanov, W. Sigle, P. Kaya, M. E. Gruner, R. Pentcheva, B. Keimer and H.-U. Habermeier, *Phys. Rev. Mater.* **3**, 085403 (2019).
32. J. Sun, M. R. Barone, C. S. Chang, M. E. Holtz, H. Paik, J. Schubert, D. A. Muller and D. G. Schlom, *APL Mater.* **7**, 121112 (2019).
33. R. Wei, P. Gong, M. Zhao, H. Tong, X. Tang, L. Hu, J. Yang, W. Song, X. Zhu and Y. Sun, *Adv. Funct. Mater.* **30**, 2002375 (2020).
34. J. M. Ok, M. Brahlek, W. S. Choi, K. M. Roccapiore, M. F. Chisholm, S. Kim, C. Sohn, E. Skoropata, S. Yoon, J. S. Kim and H. N. Lee, *APL Mater.* **8**, 051104 (2020).
35. T. Miyakawa, T. Harada, S. Ito and A. Tsukazaki, *J. Appl. Phys.* **128**, 025302 (2020).
36. G. Kästle, H.-G. Boyen, A. Schröder, A. Plettl and P. Ziemann, *Phys. Rev. B* **70**, 165414 (2004).
37. H. Hoffmann and G. Fischer, *Thin Solid Films* **36**, 25-28 (1976).
38. E. Milosevic, S. Kerdsonpanya, M. E. McGahay, A. Zangiabadi, K. Barmak and D. Gall, *J. Appl. Phys.* **125**, 245105 (2019).
39. H.-D. Liu, Y.-P. Zhao, G. Ramanath, S. P. Murarka and G.-C. Wang, *Thin Solid Films* **384**, 151-156 (2001).
40. T. Zhou and D. Gall, *Phys. Rev. B* **97**, 165406 (2018).
41. K. Fuchs, *Mathematical Proceedings of the Cambridge Philosophical Society* **34**, 100-108 (1938).
42. E. H. Sondheimer, *Adv. Phys.* **1**, 1 (1952).
43. Z. Tešanović and M. V. Jarić, *Phys. Rev. Lett.* **57**, 2760-2763 (1986).
44. N. Trivedi and N. W. Ashcroft, *Phys. Rev. B* **38**, 12298 (1988).
45. D. Calecki, *Phys. Rev. B* **42**, 6906-6915 (1990).
46. N. W. Ashcroft and N. D. Mermin, *Solid State Physics*. (Thomson Learning, Inc., the United States of America, 1976).
47. G. Baker, T. W. Branch, J. Day, D. Valentini, M. Oudah, P. McGuinness, S. Khim, P. Surówka, R. Moessner, J. Schmalian, A. P. Mackenzie and D. A. Bonn, arXiv:2204.14239 (2022).
48. N. Wolff, T. Schwaigert, D. Siche, D. G. Schlom and D. Klimm, *J. Cryst. Growth* **532**, 125426 (2020).
49. J. M. Ok, S. Yoon, A. R. Lupini, P. Ganesh, A. Huon, M. F. Chisholm and H. N. Lee, *ACS Appl. Mater. Interfaces* **13**, 22059-22064 (2021).
50. T. Harada, Unpublished results.
51. D. J. Hagen, J. Yoon, H. Zhang, B. Kalkofen, M. Silinskas, F. Börmert, H. Han and S. S. P. Parkin, *Advanced Materials Interfaces*, 220013 (2022).
52. P. W. Tasker, *J. Phys. C: Solid State Phys.* **12**, 4977-4984 (1979).
53. C. M. Yim, D. Chakraborti, L. C. Rhodes, S. Khim, A. P. Mackenzie and P. Wahl, *Sci. Adv.* **7**, eabd7361 (2021).
54. H. B. Michaelson, *J. Appl. Phys.* **48**, 4729 (1977).
55. T. Harada, S. Ito and A. Tsukazaki, *Sci. Adv.* **5**, eaax5733 (2019).

56. T. Harada and A. Tsukazaki, *APL Mater.* **8**, 041109 (2020).
57. T. Harada and A. Tsukazaki, *Appl. Phys. Lett.* **116**, 232104 (2020).
58. C. Noguera, *J. Phys.: Condens. Matter* **12**, R367-R410 (2000).
59. T. Higuchi and H. Y. Hwang, in *Multifunctional Oxide Heterostructures*, edited by E. Y. Tsymlal, E. R. A. Dagotto, C. B. Eom and R. Ramesh (Oxford University Press, 2012), pp. 183-213.
60. K. Kim, H. C. Choi and B. I. Min, *Phys. Rev. B* **80**, 035116 (2009).
61. J. H. Lee, T. Harada, F. Trier, L. Marcano, F. Godel, S. Valencia, A. Tsukazaki and M. Bibes, *Nano Lett.* **21**, 8687-8692 (2021).
62. F. Trier, P. Noël, J.-V. Kim, J.-P. Attané, L. Vila and M. Bibes, *Nature Reviews Materials* (2021).
63. J. D. Sau, R. M. Lutchyn, S. Tewari and S. D. Sarma, *Phys. Rev. Lett.* **104**, 040502 (2010).
64. A. Yamakage, Y. Tanaka and N. Nagaosa, *Phys. Rev. Lett.* **108**, 087003 (2012).
65. M. F. Crommie, C. P. Lutz and D. M. Eigler, *Nature* **363**, 524-527 (1993).
66. Y. Hasegawa and P. Avouris, *Phys. Rev. Lett.* **71**, 1071 (1993).
67. J. E. Hoffman, K. McElroy, D.-H. Lee, K. M. Lang, H. Eisaki, S. Uchida and J. C. Davis, *Science* **297**, 1148-1151 (2002).
68. T. Zhang, P. Cheng, X. Chen, J.-F. Jia, X. Ma, K. He, L. Wang, H. Zhang, X. Dai, Z. Fang, X. Xie and Q.-K. Xue, *Phys. Rev. Lett.* **103**, 266803 (2009).
69. P. Roushan, J. Seo, C. V. Parker, Y. S. Hor, D. Hsieh, D. Qian, A. Richardella, M. Z. Hasan, R. J. Cava and A. Yazdani, *Nature* **460**, 1106-1109 (2009).
70. B. Jäck, Y. Xie, B. A. Bernevig and A. Yazdani, *Proc. Natl. Acad. Sci. U.S.A.* **117**, 16214-16218 (2020).
71. P. Kong, G. Li, Z. Yang, C. Wen, Y. Qi, C. Felser and S. Yan, arXiv:2111.10062 (2021).
72. F. Mazzola, C.-M. Yim, V. Sunko, S. Khim, P. Kushwaha, O. J. Clark, L. B. I. Marković, D. Chakraborti, T. K. Kim, M. Hoesch, A. P. Mackenzie, P. Wahl and P. D. C. King, *npj Quantum Materials* **7**, 20 (2022).
73. S. E. Barnes, J. i. Ieda and S. Maekawa, *Sci. Rep.* **4**, 4105 (2014).
74. O. Krupin, G. Bihlmayer, K. Starke, S. Gorovikov, J. E. Prieto, K. Döbrich, S. Blügel and G. Kaindl, *Phys. Rev. B* **71**, 201403 (2005).
75. R. Wiesendanger, *Rev. Mod. Phys.* **81**, 1495 (2009).
76. C. Hanneken, F. Otte, A. Kubetzka, B. Dupé, N. Romming, K. v. Bergmann, R. Wiesendanger and S. Heinze, *Nature Nanotechnology* **10**, 1039-1042 (2015).
77. M. Bode, S. Heinze, A. Kubetzka, O. Pietzsch, X. Nie, G. Bihlmayer, S. Blügel and R. Wiesendanger, *Phys. Rev. Lett.* **89**, 237205 (2002).
78. Y. Yasui, C. J. Butler, N. D. Khanh, S. Hayami, T. Nomoto, T. Hanaguri, Y. Motome, R. Arita, T.-h. Arima, Y. Tokura and S. Seki, *Nat. Commun.* **11**, 5925 (2020).
79. V. Eyert, R. Frésard and A. Maignan, *Chem. Mater.* **20**, 2370-2373 (2008).
80. K. I. Bolotin, K. J. Sikes, Z. Jiang, M. Klima, G. Fudenberg, J. Hone, P. Kim and H. L. Stormer, *Solid State Communications* **146**, 351-355 (2008).
81. L. Banszerus, M. Schmitz, S. Engels, M. G. K. Watanabe, T. Taniguchi, B. Beschoten and C. Stampfer, *Nano Lett.* **16**, 1387-1391 (2016).
82. R. O. Dillon, I. L. Spain, J. A. Woollam and W. H. Lowrey, *J. Phys. Chem. Solids* **39**, 907-922 (1978).
83. D. D. L. Chung, *Journal of Materials Science* **37**, 1475-1489 (2002).
84. N. García, P. Esquinazi, J. Barzola-Quiquia, B. Ming and D. Spodig, *Phys. Rev. B* **78**, 035413 (2008).
85. L. Pfeiffer, K. W. West, H. L. Stormer and K. W. Baldwin, *Appl. Phys. Lett.* **55**, 1888 (1989).
86. V. Umansky, M. Heiblum, Y. Levinson, J. Smet, J. Nübler and M. Dolev, *J. Cryst. Growth* **311**, 1658-1661 (2009).
87. T. M. Lu, D. C. Tsui, C.-H. Lee and C. W. Liu, *Appl. Phys. Lett.* **94**, 182102 (2009).
88. J. Falson and M. Kawasaki, *Rep. Prog. Phys.* **81**, 056501 (2018).
89. I. P. Smorchkova, L. Chen, T. Mates, L. Shen, S. Heikman, B. Moran, S. Keller, S. P. DenBaars, J. S. Speck and U. K. Mishra, *J. Appl. Phys.* **90**, 5196-5201 (2001).
90. M. J. Manfra, K. W. Baldwin, A. M. Sergent, R. J. Molnar and J. Caissie, *Appl. Phys. Lett.* **85**, 1722-1724 (2004).
91. F. Trier, K. V. Reich, D. V. Christensen, Y. Zhang, H. L. Tuller, Y. Chen, B. I. Shklovskii and N. Pryds, *Appl. Phys. Lett.* **111**, 092106 (2017).
92. N. Koirala, M. Brahlek, M. Salehi, L. Wu, J. Dai, J. Waugh, T. Nummy, M.-G. Han, J. Moon, Y. Zhu, D. Dessau, W. Wu, N. P. Armitage and S. Oh, *Nano Lett.* **15**, 8245-8249 (2015).
93. S. M. Sze and K. K. Ng, *Physics of Semiconductor Devices*. (Wiley, Hoboken, 2006).
94. K. Jacobi, G. Zwicker and A. Gutmann, *Surface Science* **141**, 109-125 (1984).
95. S. Y. Davydov, *Semiconductors* **41**, 696-698 (2007).
96. S.-C. Lin, C.-T. Kuo, X. Liu, L.-Y. Liang, C.-H. Cheng, C.-H. Lin, S.-J. Tang, L.-Y. Chang, C.-H. Chen and S. Gwo, *Applied Physics Express* **5**, 031003 (2012).
97. S. J. Pearton, J. Yang, P. H. Cary IV, F. Ren, J. Kim, M. J. Tadjer and M. A. Mastro, *Applied Physics Reviews* **5**, 011301 (2018).
98. M. Mohamed, K. Irmscher, C. Janowitz, Z. Galazka, R. Manzke and R. Fornari, *Appl. Phys. Lett.* **101**, 132106 (2012).
99. K. G. Crawford, I. Maini, D. A. Macdonald and D. A. J. Moran, *Prog. Surf. Sci.* **96**, 100613 (2021).
100. F. Maier, J. Ristein and L. Ley, *Phys. Rev. B* **64**, 165411 (2001).